



**HAL**  
open science

# Growth couples temporal and spatial fluctuations of tissue properties during morphogenesis

Antoine Fruleux, Lilan Hong, Adrienne Roeder, Chun-Biu Li, Arezki Boudaoud

► **To cite this version:**

Antoine Fruleux, Lilan Hong, Adrienne Roeder, Chun-Biu Li, Arezki Boudaoud. Growth couples temporal and spatial fluctuations of tissue properties during morphogenesis. Proceedings of the National Academy of Sciences of the United States of America, 2024, 121 (23), 10.1073/pnas.2318481121 . hal-04798455

**HAL Id: hal-04798455**

**<https://hal.science/hal-04798455v1>**

Submitted on 22 Nov 2024

**HAL** is a multi-disciplinary open access archive for the deposit and dissemination of scientific research documents, whether they are published or not. The documents may come from teaching and research institutions in France or abroad, or from public or private research centers.

L'archive ouverte pluridisciplinaire **HAL**, est destinée au dépôt et à la diffusion de documents scientifiques de niveau recherche, publiés ou non, émanant des établissements d'enseignement et de recherche français ou étrangers, des laboratoires publics ou privés.



# Growth couples temporal and spatial fluctuations of tissue properties during morphogenesis

Antoine Fruleux<sup>a,b,c,1</sup> , Lilan Hong<sup>d</sup>, Adrienne H. K. Roeder<sup>e</sup> , Chun-Biu Li<sup>f</sup> , and Arezki Boudaoud<sup>a,b,1</sup> 

Edited by Michael Moshe, Hebrew University of Jerusalem—Edmond J. Safra Campus, Jerusalem, Israel; received October 23, 2023; accepted April 27, 2024 by Editorial Board Member Mehran Kardar

Living tissues display fluctuations—random spatial and temporal variations of tissue properties around their reference values—at multiple scales. It is believed that such fluctuations may enable tissues to sense their state or their size. Recent theoretical studies developed specific models of fluctuations in growing tissues and predicted that fluctuations of growth show long-range correlations. Here, we elaborated upon these predictions and we tested them using experimental data. We first introduced a minimal model for the fluctuations of any quantity that has some level of temporal persistence or memory, such as concentration of a molecule, local growth rate, or mechanical property. We found that long-range correlations are generic, applying to any such quantity, and that growth couples temporal and spatial fluctuations, through a mechanism that we call “fluctuation stretching”—growth enlarges the length scale of variation of this quantity. We then analyzed growth data from sepals of the model plant *Arabidopsis* and we quantified spatial and temporal fluctuations of cell growth using the previously developed cellular Fourier transform. Growth appears to have long-range correlations. We compared different genotypes and growth conditions: mutants with lower or higher response to mechanical stress have lower temporal correlations and longer-range spatial correlations than wild-type plants. Finally, we used theoretical predictions to merge experimental data from all conditions and developmental stages into a unifying curve, validating the notion that temporal and spatial fluctuations are coupled by growth. Altogether, our work reveals kinematic constraints on spatiotemporal fluctuations that have an impact on the robustness of morphogenesis.

morphogenesis | growth variability | multiscale | robustness | living tissues

The impact of noisy perturbations on organism development is the subject of active research (1). Fluctuations—the random spatial and temporal variations of tissue properties around their reference values—have been observed at multiple scales, from cytoskeleton (2) to cell (3) and tissue (4). In the fruit fly, for example, actomyosin pulses were shown to cause fluctuations of cell shape (5–7), while fluctuations of the position of cell junctions were found to favor cell rearrangements during tissue extension (8, 9). It was proposed that fluctuations are required for symmetry breaking and pattern formation during development (10, 11) or for cells and tissues to sense their neighborhood (12). Fluctuations in gene expression or morphogens seem particularly important for cell differentiation. Fluctuations in gene transcription seem required for the maintenance of pluripotency (13, 14), and specific properties of fluctuations are a signature of cell differentiation (15–18). Nevertheless, the robustness of tissue patterning appears sensitive to fluctuations in molecule concentrations (19, 20). Growth variability induces mechanical stress (12, 21–23) because, for instance, cells with higher growth rate exert forces on neighboring cells, which may sense and respond to such mechanical stress. Robust development of the fruit fly wing partially relies on cell competition, i.e., on mismatch of growth rates between cells, and on the ensuing modulation of proliferation and apoptosis (24, 25). In this context, it is important to understand whether fluctuations of a cell affect its local neighborhood or the whole tissue. Here, we analyzed the spatial structure of fluctuations in experimental data from growing tissues.

Recent models of tissue mechanics and growth accounted for temporal and spatial fluctuations of growth and investigated their role in robustness of morphogenesis (26–28). Temporal fluctuations are characterized by their degree of persistence, quantified with the persistence time (or correlation time), the characteristic time over which memory of previous fluctuations is lost. It could be the time needed for remodeling of the cytoskeleton or of the extracellular matrix (in animals)/the cell wall (in plants). Spatial fluctuations are characterized by their degree of spatial consistency, quantified by the correlation length, the characteristic length over which cells (or subcellular domains) behave similarly, or by

## Significance

How do organs and organisms grow and achieve robust shapes in the face of subcellular and cellular variability? In order to address this outstanding mystery, we investigated the variability of growth at multiple scales and we analyzed experimental data from growing plant tissues. Our results support the prediction that tissue expansion couples temporal memory of growth with spatial variability of growth. Our work reveals a constraint on the spatial and temporal variability of growth that may impact the robustness of morphogenesis.

Author contributions: A.F. and A.B. designed research; A.F. performed research; A.F. contributed new reagents/analytic tools; A.F. and L.H. analyzed data; A.H.K.R., C.-B.L., and A.B. supervision and funding; and A.F., A.H.K.R., C.-B.L., and A.B. wrote the paper.

The authors declare no competing interest.

This article is a PNAS Direct Submission. M.M. is a guest editor invited by the Editorial Board.

Copyright © 2024 the Author(s). Published by PNAS. This article is distributed under [Creative Commons Attribution-NonCommercial-NoDerivatives License 4.0 \(CC BY-NC-ND\)](https://creativecommons.org/licenses/by-nc-nd/4.0/).

<sup>1</sup>To whom correspondence may be addressed. Email: antoine.fruleux@universite-paris-saclay.fr or arezki.boudaoud@polytechnique.edu.

This article contains supporting information online at <https://www.pnas.org/lookup/suppl/doi:10.1073/pnas.2318481121/-/DCSupplemental>.

Published May 30, 2024.

cell-to-cell variability over a small neighborhood. For instance, the shape of a plant organ was found to be less robust in a mutant with lower cell-to-cell variability (26). However, spatial fluctuations may have a more complex structure. Indeed, theoretical models of the expanding universe (29, 30) and of growing tissues (27, 28) predicted long-range spatial correlations, i.e., a significant level of correlations between fluctuations of two distant parts of the system; accordingly, growing systems are expected to exhibit fluctuations at multiple scales. Here, we focus on the underlying mechanism, which we call fluctuation stretching—the increase in the length scale of fluctuations of a tissue property or of the concentration of a molecule, due to tissue expansion.

To assess the experimental relevance of this mechanism, we analyzed growth fluctuations in the model plant *Arabidopsis thaliana*. We considered the sepal, the green leaf-like organ that protects a flower prior to its opening. We characterized sepals from wild-type individuals in different culture conditions as well as mutant plants. We considered *spiral2* and *katanin* mutant plants since they were found to be less robust to variability in the number of trichomes (epidermal hair-like cells) than wild-type plants (31), suggesting a greater impact of cellular scales on organ ones. The lack of SPIRAL2 and KATANIN function led respectively to stronger (31–33) and weaker (31, 32, 34) cortical microtubule coalignment and reorientation in response to mechanical stress (35, 36). Microtubules guide the deposition of cellulose fibers in the cell wall (the plant extracellular matrix) (37). Cellulose fibers being the main load-bearing component of the cell wall, the response of microtubules to mechanical stress is generally considered as a mechanical feedback on growth and *spiral2* and *katanin* as mutants with altered feedback.

In this article, we first present a simple model for fluctuation stretching. We estimate spatial and temporal correlations of tissue growth fluctuations in *Arabidopsis* sepals using previous live imaging data (31, 32) and the cellular Fourier transform (CFT) (38). We investigate how correlations vary within and between datasets, and we test the relevance of fluctuation stretching.

## Results

**A Minimal Model Predicts the Stretching of Fluctuations in Growing Tissues.** Fluctuation stretching, the enlargement of the length scales of fluctuations by medium expansion, was predicted by different models of expanding media, the early universe (29, 30) and living tissues (27, 28). Here, we introduce a minimal model for fluctuation stretching. For a reader primarily interested in experimental data, Eq. 2 is the main theoretical result that we test in growing sepals.

We consider a variable property  $\Phi$  that is defined on a tissue growing isotropically at average rate  $\bar{G}$  and that depends on position vector  $x$  and time  $t$ . This variable  $\Phi$  could reflect gene expression, signaling, metabolism, cell size, or cell growth, for instance. We assume that i)  $\Phi$  is inherited during tissue growth, so that it is advected (transported) by the average growth velocity  $\bar{G}x/D$  ( $D$  is the space dimension:  $D = 1$  in Figs. 1 and 2 and  $D = 2$  for a thin organ like the sepal), ii)  $\Phi$  relaxes to its average value  $\langle \Phi \rangle$  with a characteristic memory (persistence/correlation) time  $\tau$ , and iii)  $\Phi$  is subject to a source of noise  $\xi(x, t)$  that is random in space and time. As a consequence,

$$\frac{\partial \Phi}{\partial t} + \frac{\bar{G}x}{D} \cdot \frac{\partial \Phi}{\partial x} = -\frac{1}{\tau} (\Phi(x, t) - \langle \Phi \rangle) + \xi(x, t). \quad [1]$$

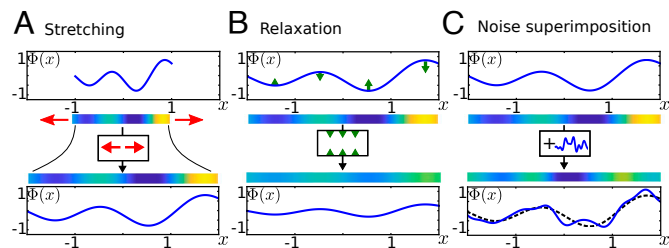


**Fig. 1.** Distinct effects of tissue expansion, time relaxation (loss of memory), and noise source on the spatial pattern of a tissue property. The figure shows initial spatial patterns and their temporal evolution under the three mechanisms. The variable property  $\Phi(x)$  is plotted as a function of position  $x$  and shown in colorscale (blue and yellow for low and high values, respectively) along a strip standing for the growing tissue. (A) Tissue expansion induces fluctuation stretching, defined as the enlargement of the length scales of fluctuations. (B) Relaxation associated with loss of memory induces a decay in the amplitude of fluctuations (depicted by green arrows). (C) Noise causes the superimposition of new fluctuations on the preceding pattern (represented by a dashed line in the *Lower* panel). We schematically represent stretching, relaxation, and noise superimposition by function block diagrams containing horizontal red arrows, vertical green arrows, and a noisy signal, respectively. These block diagrams are used in Fig. 2.

In this equation, the first term is the temporal derivative of  $\Phi(x, t)$ . The second term (on the right-hand side) represents the effect of tissue expansion, i.e., advection by growth, and contains the spatial derivative of  $\Phi$  (the dot  $\cdot$  stands for the vectorial product, which reduces to a multiplication for  $D = 1$ ). The third term (left-hand side) describes relaxation (loss of memory) of  $\Phi$ .

The consequences of tissue expansion, loss of memory (time persistence), and noise on the variations of  $\Phi$  are schematized in Fig. 1, for one time step. Tissue expansion induces “fluctuation stretching,” i.e., enlarges the length scales of spatial variations (panel A). Time persistence determines how fast fluctuations relax toward their reference level (B). Noise superimposes new fluctuations on the preceding pattern (C).

When iterated over time, fluctuation stretching and noise give rise to multiscale fluctuations, while the degree of time persistence (or memory level) controls how far fluctuations extend toward large space-scales. This is illustrated in Fig. 2A. In three regimes: for full, intermediate, and vanishing time persistence. For full-time persistence ( $\tau \bar{G} = +\infty$ ), the pattern is stretched, increasing the length scale of variations of  $\Phi$ , and fluctuations are added at small scale. For intermediate time persistence ( $\tau \bar{G} \sim 1$ ), the same process occurs but the preexisting pattern is attenuated due to relaxation. In the absence of temporal persistence ( $\tau = 0$ ), the preceding pattern disappears and only the newly superimposed noise remains. Mathematically, the solutions to Eq. 1 take the form  $\Phi(x, t) = \langle \Phi \rangle + \int_0^{+\infty} ds e^{-s/\tau} \xi(x e^{-s\bar{G}/D}, t - s)$  (see *SI Appendix, Supplementary Note* for details). The integral indicates the superimposition while the exponential factor  $e^{-s/\tau}$  accounts for time relaxation or loss of memory. Fluctuation stretching corresponds to the exponential factor  $e^{s\bar{G}/D}$  applied to the spatial variation of the noise.

The space correlation function,  $C(l)$ , is the pairwise correlation between the values  $\Phi(x)$  and  $\Phi(x + l)$  of the variable  $\Phi$  at positions distant of length  $l$ , as illustrated in Fig. 2B.  $C(l)$  generally decreases with the distance  $l$ : For  $l = 0$ ,  $\Phi(x) = \Phi(x + l)$  and so the correlation is complete,  $C(0) = 1$ , while at large distance  $l$ ,  $\Phi(x + l)$  is expected to be independent of  $\Phi(x)$  and the correlation vanishes as illustrated in the plot on the *Right* of panel B. In our minimal model, the correlation function takes the form  $C(l) = \int_0^{+\infty} (2 ds/\tau) e^{-2s/\tau} g(|l| e^{-s\bar{G}/D})$ , assuming

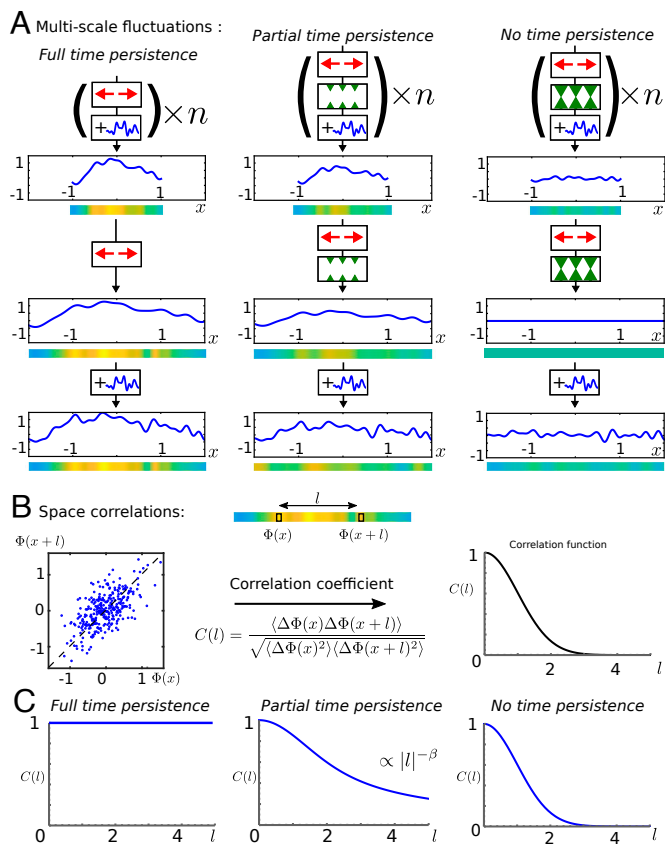


**Fig. 2.** Multiscale fluctuations as a consequence of fluctuation stretching. Spatial correlations of tissue properties depend on the level of temporal persistence of fluctuations. Three levels of temporal persistence are considered: full (no time relaxation), intermediate (moderate relaxation), and none (instantaneous relaxation). (A) Spatial pattern resulting from the iteration of fluctuation stretching, relaxation, and noise, schematically represented by function block diagrams in series, as defined in Fig. 1; patterns are represented under the form of plots and color stripes as in Fig. 1. *Top*: patterns after  $n$  iterations; *Middle*: patterns after one additional iteration of stretching and (if appropriate) relaxation; *Bottom*: patterns after one additional superimposition of noise. (B) Quantification of spatial correlations. *Top*: This involves comparing the values of the variable at positions  $x$  and  $x+l$ , as illustrated in the colored strip. *Left*: Typical scatter plot showing  $\Phi(x+l)$  as a function of  $\Phi(x)$  for multiple values of  $x$ . *Middle*:  $C(l)$  is defined as the correlation coefficient between  $\Phi(x+l)$  and  $\Phi(x)$ ;  $\langle \rangle$  stands for the statistical average of the expression between brackets and the fluctuation around average  $\Delta\Phi(x) = \Phi(x) - \langle \Phi(x) \rangle$ . *Right*: the correlation  $C(l)$  as a function of the distance  $l$ . (C) Spatial correlation function  $C(l)$  for full, partial, and no time persistent fluctuations. Models predict that the space correlation function is a power-law of  $l$ ,  $C(l) \propto l^{-\beta}$ .

the permanent noise source  $\langle \xi(x, t) \rangle = 0$  has zero mean and correlation function  $\langle \xi(x, t)\xi(x+l, t+s) \rangle$  proportional to  $\delta(s)g(l)$  ( $\delta$  is the Dirac distribution; see *SI Appendix, Supplementary Note* for details). Here again  $C(l)$  appears as a weighted sum of the space correlation function  $g$  of the noise source stretched at different spatial scales. The correlation function  $g$  is assumed to have a correlation length  $\ell$  that sets the reference scale for spatial variations of  $\Phi$ ;  $\ell$  cannot be assumed to be zero without causing issues of mathematical convergence. In practice, we took  $g(l) = e^{-|l|^2/(2\ell^2)}(2\pi\ell^2)^{-D/2}$ . Because of fluctuation stretching, space correlations functions for time persistent fluctuations are predicted to be long-ranged, i.e., to have their tails which follow a power law  $\propto l^{-\beta}$ . As shown in *SI Appendix, Supplementary Note*, this can be made explicit by rewriting the space correlation function  $C(l) = |l|^{-2D/(\tau\bar{G})}b(|l|)$ , where

the increasing function  $b(|l|) = \int_0^{|l|} du u^{2D/(\tau\bar{G})-1}g(u)$  reaches an asymptotic value when  $|l|$  becomes large compared to the correlation length  $\ell$  of  $\xi$ . Therefore, the correlation function  $C(l)$  of the variable of interest  $\Phi$  mostly behaves as a power-law  $C(l) \sim l^{-\beta}$  of exponent

$$\beta = \frac{2D}{\tau\bar{G}}. \quad [2]$$

This scaling law indicates that the values of the variable  $\Phi$  considered in two distant points decorrelate slowly as their distance is increased, which reflects the fact that fluctuations are a superimposition of patterns with different spatial length scales.  $\beta$  estimates this spatial decrease in correlations, the higher the memory (the larger  $\tau\bar{G}$ ), the higher correlations between distant regions. Fig. 2C show the space correlation functions for full, partial, and no memory. Full temporal persistence is simply the limit where the persistence time is infinite, leading to an accumulation of fluctuations at large length scales. The weight of large-scale fluctuations continuously increases so that the correlation function tends toward a constant. In contrast, in the absence of temporal persistence, spatial correlations vanish beyond the correlation length of the noise. Hereafter, we tested this prediction using previous experimental data about growing plant organs.

### Live Imaging and Spectral Analysis Provide Estimates for Spatiotemporal Correlations of Cell Growth.

Next, we aimed at a quantitative description of spatial and temporal correlations of growth fluctuations in expanding tissues. We used experimental data where sepals were imaged live to track morphogenesis over time, with similar culture and imaging conditions (31, 32). We examined whether fluctuations stretching applies to cell areal growth rate. Each sepal was imaged at multiple times, labeled  $t = 0, 1, 2, \dots$  and separated by 24 h intervals as illustrated by Fig. 3A, which shows an example of cells segmented in a sepal, at three successive time steps  $t, t+1$ , and  $t+2$ . Growth was defined from cell surface area at successive time steps. Fig. 3B shows cell areal relative growth rate  $G_{i,t}$  and  $G_{i,t+1}$  from  $t$  to  $t+1$  and from  $t+1$  to  $t+2$ , respectively, deduced from segmentation of sepals into cells, as showed in panel A and mapped on the reference tissues at  $t$  and  $t+1$ , respectively. When a cell has divided between  $t$  and  $t+1$ , we used the total surface area of its daughter cells at  $t+1$  to define  $G_{i,t}$ ; see *Datasets and Methods* for details.

To dissect spatial variations of growth in the tissue, we used the CFT (38). The CFT consists of decomposing the signal into a linear combination of ad hoc harmonics that account for the subdivision of the tissue into cells of variable size and shape. These harmonics are the equivalent of sinusoidal waves in an infinite continuous medium. The  $k$ -th harmonic,  $e_k$ , has wavenumber  $q_k$ , and varies on a length scale that decreases with the rank  $k$ . The CFT coefficients  $\hat{G}_{k,t}$  give the weights with which cell relative areal growth is decomposed into the harmonics  $e_k$ . The Fourier spectrum is obtained by plotting the amplitude  $|\hat{G}_{k,t}|$  as a function of the corresponding wave number  $q_k$ . This spectrum is well suited to describe fluctuations of  $G$  at multiple scales.

We investigated spatial correlations from Fourier spectra such as those shown in Fig. 3D. The amplitudes of spectra appear significantly higher for low wave numbers, suggesting long-range correlations. To further test this, we sought a characteristic length scale for fluctuations and we considered the smallest index  $K$  for which  $\sum_{k=1}^K \hat{G}_k^2 \geq 1/2 \sum_{k=1}^{N-1} \hat{G}_k^2$ , so as to quantify

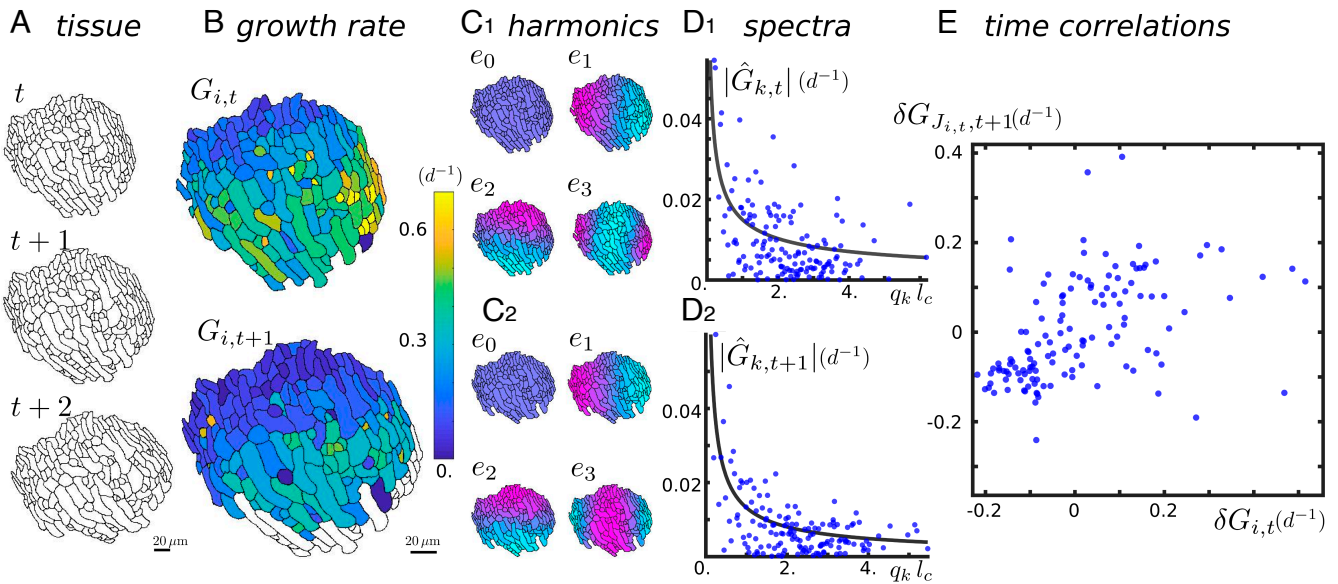


**Fig. 3.** Quantification of spatial and temporal fluctuations in cell growth. Day ( $d$ ) is used as a unit of time. (A) Three snapshots of a plant tissue (abaxial sepal epidermis from wild-type plant) taken at one-day intervals. Black lines represent cell contours. (B) Heatmaps of relative areal growth rate between times  $t$  and  $t + 1$ ,  $G_{i,t}$ , and between  $t + 1$  and  $t + 2$ ,  $G_{i,t+1}$  for cell  $\#i$ . A growth rate of  $1d^{-1}$  corresponds to a relative increase of area of 100% in 1 d. Growth rate of white cells could not be computed because they were not imaged at  $t + 2$ . (C<sub>1</sub> and C<sub>2</sub>) The first four harmonics  $e_k$  ( $k = 0, 1, 2$ , and  $3$ ) of the CFT of the tissue at  $t$  and  $t + 1$  (the white cells in (B) are not included), represented by a cyan (low value) to magenta (high values) color scheme. The harmonics  $e_k$  generalize sinusoidal waves and can be used to decompose the growth fields  $G_{i,t}$  and  $G_{i,t+1}$  into their respective CFTs  $\hat{G}_{k,t}$  and  $\hat{G}_{k,t+1}$ . (D<sub>1</sub> and D<sub>2</sub>) Fourier spectra (blue dots) correspond to the absolute values  $|\hat{G}_{k,t}|$  and  $|\hat{G}_{k,t+1}|$  of the CFTs and are shown as function of the wavenumber  $q_k$  of the harmonics  $e_k$ . Wavenumbers were nondimensionalized using mean cell size  $l_c$ . A representative power-law (solid line)  $\Delta G_t q_k^{-\alpha_t} / (\sum_k q_k^{-2\alpha_t})^{1/2}$  was obtained as explained in the text. Each spectrum is then characterized by two numbers, the SD of cell growth  $\Delta G_t$  and the spatial exponent of spatial correlations,  $\alpha_t$ . Here,  $\alpha_t = 0.54 \pm 0.08$  ( $\pm$ SE of the mean),  $\alpha_{t+1} = 0.71 \pm 0.08$ ,  $\Delta G_t = 0.157 \pm 0.012 d^{-1}$  and  $\Delta G_{t+1} = 0.134 \pm 0.012 d^{-1}$ . (E) For temporal analyses, detrended areal growth rate  $\delta G_{i,t}$  was computed as the excess areal growth rate of a cell with respect to a local neighborhood. The coordinates of each blue dot are the detrended growth  $\delta G_{i,t}$  of a cell  $i$  between  $t$  and  $t + 1$  (horizontal axis) and the detrended growth  $\delta G_{J_{i,t},t+1}$  of the set  $J_{i,t}$  of its daughters between  $t + 1$  and  $t + 2$  (vertical axis). The degree of growth temporal correlation is quantified by the value of the Kendall correlation coefficient; here,  $\Gamma_t = 0.400 \pm 0.052$  ( $\pm$ SE). Two outliers were excluded from the plot to improve the readability of the figure.

the repartition of fluctuations between low and large scales. If fluctuations were short-ranged, then the ratio of largest to characteristic wavenumbers,  $q_1/q_K$ , would be a good estimate of the ratio of correlation length to sample size, and would therefore be small compared to 1. In contrast, we found the ratio  $q_1/q_K$  to be 0.54 on average (SD 0.29 and range 0.086 to 1, over all study samples), indicating long-range correlations. This qualitative agreement with the predictions of the minimal model prompted us to use power-laws to represent Fourier spectra. We note that the prediction  $C(l) \sim l^{-\beta}$  corresponds to a spectrum scaling like  $q^{-\alpha}$ , with  $\alpha = 1 - \beta/2$  (Datasets and Methods). Although the limited range of wavenumbers did not allow us to test the power-law behavior, we obtained a representative power-law as follows. As the CFTs can be positive or negative, we assumed each CFT to follow a Gaussian distribution of zero mean and of SD  $\sigma_{k,t}$ , which was fitted to the equation  $\Delta G_t q_k^{-\alpha_t} / (\sum_k q_k^{-2\alpha_t})^{1/2}$ . Each spectrum is then characterized by two numbers, its amplitude  $\Delta G_t$  and its exponent,  $\alpha_t$ . The specific choice made for the fit is such that, following the Parseval theorem,  $\Delta G_t$  measures the SD of growth while  $\alpha_t$  measures its spatial correlations. We used statistical inference to estimate  $\alpha_t$  and  $\Delta G_t$ . The scaling exponent,  $\alpha_t$ , is expected to vary between 0 and 1, which correspond to short-range and to extremely long-range correlations, respectively. We found  $\alpha_t$  to approximately range between 0.1 and 0.9, indicating large differences between samples and time points in terms of range of correlations (but see below for the comparison between genotypes). We found the SD of growth  $\Delta G_t$  to range between 0.1 and  $0.6 d^{-1}$ , values

that are of the order of half the growth rate of a sample averaged over all cells between two time points, indicating relatively strong fluctuations of cell growth rate.

The temporal resolution ( $1d$ ) and the number of consecutive images of a sample (3 to 7) were in general too low to compute persistence time from experimental data. We therefore estimated temporal persistence of growth using correlation coefficients. We considered the correlations between relative areal cell growth  $G_{i,t}$  from  $t$  to  $t + 1$  and  $G_{J_{i,t},t+1}$  from  $t + 1$  to  $t + 2$ , where the set  $J_{i,t}$  in subscript contains the labels of all daughters of cell  $i$  at time  $t$  and  $G_{J_{i,t},t+1}$  is their areal growth rate; see Datasets and Methods for details. To avoid any bias due to overall gradients in growth rate (32), we computed detrended cell growth  $\delta G_{i,t}$  by subtracting from the areal growth rate of a cell the average areal growth in a local neighborhood; see SI Appendix, Supplementary Note. The scatter plot in Fig. 3E of  $\delta G_{J_{i,t},t+1}$  as a function of  $\delta G_{i,t}$  shows that growth is relatively persistent in time: For instance, cells that grow more than their neighbors between  $t$  and  $t + 1$  tend to remain so between  $t + 1$  and  $t + 2$ . We quantified temporal correlations of growth using Kendall's correlation coefficient,  $\Gamma_t$ , because it is based on the rank of data and is less sensitive to outliers than the more classical rank-based Spearman correlation coefficient (39). Over all sepals and time points considered,  $\Gamma_t$  approximately ranges from  $-0.1$  to  $0.6$ . Almost all values of  $\Gamma_t$  were positive, while the negative values of  $\Gamma_t$  were not significantly different from zero (see below), indicating that, in general, growth is persistent over a time comparable to experimental time resolution ( $1d$ ).

We thus obtained a minimal set of parameters to describe growth fields and their fluctuations: average growth rate,  $\bar{G}_t$ , extent (exponent) of spatial correlations,  $\alpha_t$ , amplitude of spatial correlations,  $\Delta G_t$ , and temporal correlation coefficient  $\Gamma_t$ . Next, we analyzed differences and common features between sepals based on this minimal set of parameters.

**Temporal and Spatial Correlations of Cell Growth Vary Across Genotypes and Culture Conditions.** We analyzed growth fluctuations in several genotypes and culture conditions. As explained in the introduction, we chose to focus on mutants affected in responses to mechanical stress, *spiral2* (*spr2*) and *katanin* (two alleles, *bot1* and *mad5*), in addition to wild-type plants. We analyzed sepals from four genotypes in two culture conditions and at different developmental stages. In order to enable the comparison between several sepals that were imaged starting from different stages, we temporally aligned live imaging sequences along a common time frame using sepal width, building upon the approach developed in ref. 40; see *Datasets and Methods*. The parameters that characterize growth fields in all these sequences are shown in Fig. 4.

We first noticed a significant variability within and between genotypes/conditions and trajectories that seem heterogeneous in time. Some of this variability might be due to experimental constraints; for instance, the imaged regions of sepals varied in time and between individuals. We nevertheless observed a few trends that hold for several genotypes and conditions. Mean growth rate (panel A) decreases in time for trajectories that are long enough (*spr2*, *mad5*, and wild-type in dataset 2),

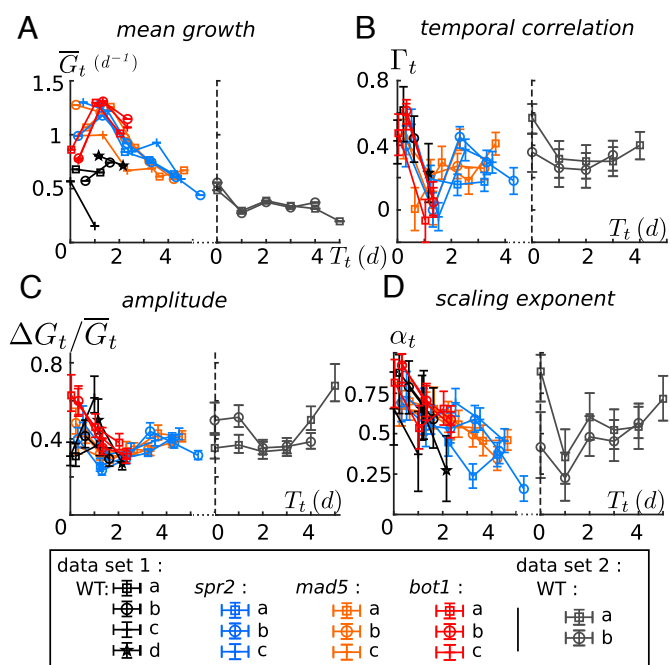


**Fig. 4.** Parameters that characterize growth fields in sepals from wild-type and mutant plants. The sequences were temporally aligned and parameters are shown as a function of the synchronized time  $T_t$ . (A) Growth rate averaged over the tissue  $\bar{G}_t$ . (B) Temporal correlation coefficient  $\Gamma_t$ . (C) Dimensionless amplitude of the CFT  $\Delta G_t / \bar{G}_t$  (also coefficient of variation of growth). (D) Scaling exponent of the CFT  $\alpha_t$ . The two datasets correspond to two slightly different culture conditions. Black, blue, orange, and red symbols/lines correspond respectively to wild-type, *spr2* mutant, *mad5* mutant, and *bot1* mutant from the first dataset, while gray symbols/lines correspond to wild-type plants from the second set. Error bars indicate the 90% CI; error bars are not shown in A because they are comparable to symbol size.

which is a general trend in organ morphogenesis. Temporal correlations (panel B) decrease between the first and the second time point, possibly associated with the strong decrease in growth anisotropy observed after the second time interval (32). The relative amplitude of growth fluctuations (panel C) decreases for the first stages in mutants before stabilizing around 0.4. The extent of spatial correlations (panel D) tends to decrease with time in dataset 1.

In order to quantify differences induced by mutations or culture conditions, we used wild-type plants from dataset 1 as a reference and we estimated the shift in growth parameters between the reference and other genotypes or culture condition; see Fig. 5. As the amount of information available varied with genotype, culture condition, or temporal stage, we developed a method that enables a consistent comparison of differences by taking into account developmental stages; see *Datasets and Methods* for details. Briefly, we considered all pairs formed by a reference sepal (wild-type from dataset 1) and another sepal. We computed the shift between a reference sepal to another sepal at a given temporal stage and we averaged shifts over time and sepal pairs to obtain a mean shift, shown in Fig. 5 for all comparisons. This mean shift can be understood as the representative vertical difference between reference wild-type curves and mutant or dataset 2 curves from Fig. 4. We then estimated the SE of these shifts, which results from the uncertainties of both reference sepals (wild-type from dataset 1) and sepals of the condition of interest.

In wild type, datasets 1 and 2 do not differ in temporal correlations (panel B) and amplitude of fluctuations (Fig. 5C) within the range of uncertainty on these parameters. Average growth rate (Fig. 5A) and extent of spatial correlations (Fig. 5D) are lower in dataset 2, indicating that these two parameters are more sensitive to culture conditions. Average growth  $\bar{G}_t$  is higher in mutants than in wild-type (Fig. 5A) over the temporal window considered; this might be compensated by lower growth in mutants at later stages or by earlier growth arrest in mutants, because mutant sepals are about 20% smaller in area than wild-type sepals (31). The amplitude of fluctuations  $\Delta G_t$  is smaller in *spiral2*, but it is not possible to conclude about *katanin*, because the two alleles (*bot1* and *mad5*) show different trends (Fig. 5C). When comparing mutants to wild-type plants, temporal correlations are lower (Fig. 5B), suggesting lower persistence time in mutants. The changes in temporal correlations  $\Gamma_t$  are lower than in growth rates, so that the changes in nondimensional persistence time  $\tau_t \bar{G}_t$  are expected to be dominated by those in growth  $\bar{G}_t$ , with higher  $\tau_t \bar{G}_t$  in mutants. This might be ascribed to differences in mechanical responses in these mutants—assuming wild-type plants to have optimal mechanical responses, both overreaction and underreaction to mechanical stress would increase the timescale of changes in growth rates (27). Based on our minimal model of fluctuation stretching (Eq. 2), smaller nondimensional persistence time  $\tau_t \bar{G}_t$  would yield higher extent  $\alpha_t$  of spatial correlations. Indeed, the exponent of the Fourier spectrum appears higher in mutants (Fig. 5D), although the level of uncertainty makes it difficult to draw a firm conclusion. In the following section, we further test whether fluctuations stretching applies to cell growth in sepals.

**A Conserved Relation between Growth Parameters Supports Fluctuation Stretching.** We sought relations between growth parameters that would hold across genotypes, datasets, and developmental stages. We first considered the pairwise relations between the growth parameters defined for each sepal: mean

## Averaged shifts from WT set 1

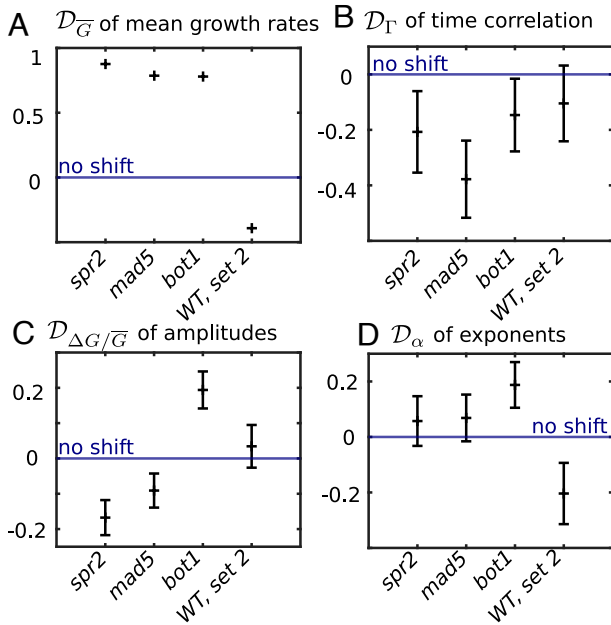


**Fig. 5.** Differences in growth parameters due to mutations or to change in culture conditions. Data are shown for mutants from dataset 1 and wild-type (WT) from dataset 2; wild-type from dataset 1 was used as a reference in all cases. Symbols show the mean shifts  $\mathcal{D}_{\bar{G}_t}$ ,  $\mathcal{D}_{\Gamma_t}$ ,  $\mathcal{D}_{\Delta G_t/\bar{G}_t}$ , and  $\mathcal{D}_{\alpha_t}$  of: (A), growth rates averaged over sepals,  $\bar{G}_t$ , (B), temporal correlation coefficients,  $\Gamma_t$ , (C), dimensionless amplitudes of growth fluctuations,  $\Delta G_t/\bar{G}_t$ , and (D), exponents quantifying spatial extents of growth fluctuations,  $\alpha_t$ , respectively. Symbols and error bars correspond to the mean and SE of the difference, respectively; error bars combine the errors on the shifts  $\mathcal{D}_\Phi$  computed from the error on the data of interest (mutants or WT dataset 2) and on the reference one (WT dataset 1).

growth rate,  $\bar{G}_t$ , temporal correlation coefficient,  $\Gamma_t$ , normalized amplitude of spatial fluctuations,  $\Delta G_t/\bar{G}_t$ , and extent (exponent) of spatial fluctuations,  $\alpha_t$ . The corresponding scatter plots are shown in Fig. 6 A–F. To assess these pairwise relations, we computed Kendall’s correlation coefficient between pairs of parameters. We found rather weak trends overall. The strongest trends were between the exponent,  $\alpha_t$ , and the temporal correlation coefficient,  $\Gamma_t$ , and between  $\alpha_t$  and the average growth  $\bar{G}_t$ . Interestingly, these trends are consistent with fluctuation stretching: larger spatial extent of fluctuations is favored by higher growth rate and by higher temporal persistence; see Eq. 2. We therefore tested more directly the predictions of fluctuation stretching.

Fluctuation stretching does not reduce to a pairwise relation between growth parameters because it relates spatial correlations to time persistence and growth rate. If this phenomenon is at play in sepals, then Eq. 2 and the relation  $\alpha = 1 - \beta/2$  (*Datasets and Methods*) imply  $\alpha_t = 1 - 2/(\tau_t \bar{G}_t)$ , where  $\tau_t$  is the persistence time. We could measure all parameters of this relation but  $\tau_t$ . Nevertheless the temporal correlation coefficient,  $\Gamma_t$ , should be a decreasing function of  $\Delta t/\tau_t$ ,  $\Gamma_t = f(\Delta t/\tau_t)$ , where  $f$  is an unknown function and  $\Delta t = 1d$  is the time delay between two steps of live imaging, because correlations between states of the sepal at consecutive time steps are higher if the time delay is small compared to the persistence time. By eliminating  $\tau_t$  from the preceding equations, we found that the time correlation coefficient depends on a combination of the other parameters,

$$\Gamma_t = f(\Delta t \bar{G}_t (1 - \alpha_t)/2). \quad [3]$$

We plotted in Fig. 6G the time correlation coefficient  $\Gamma_t$  as a function of  $\Delta t \bar{G}_t (1 - \alpha_t)/2$ . The trend is much clearer than in all other panels of Fig. 6 (Kendall’s coefficient  $\kappa = -0.48$ ) and the data seem to collapse along a line. We used statistical inference to perform a linear fit of the data,  $\Gamma_t = \beta_0 + \beta_1 \Delta t \bar{G}_t (1 - \alpha_t)/2$ ; see *SI Appendix, Supplementary Note*. We obtained fit parameters  $\beta_0 = 0.596 \pm 0.024$  and  $\beta_1 = -1.87 \pm 0.15$ , with relatively small SDs. We then confirmed with a Kolmogorov–Smirnov test that the residuals (the spread of the data around the fit) could be explained by the uncertainty on the estimates of  $\tau_t$  and  $\Gamma_t$  (*SI Appendix, Supplementary Note*), while the same analysis for the other plots (Fig. 6 A–F) confirmed that none of these plots was consistent with a linear behavior. Altogether these results

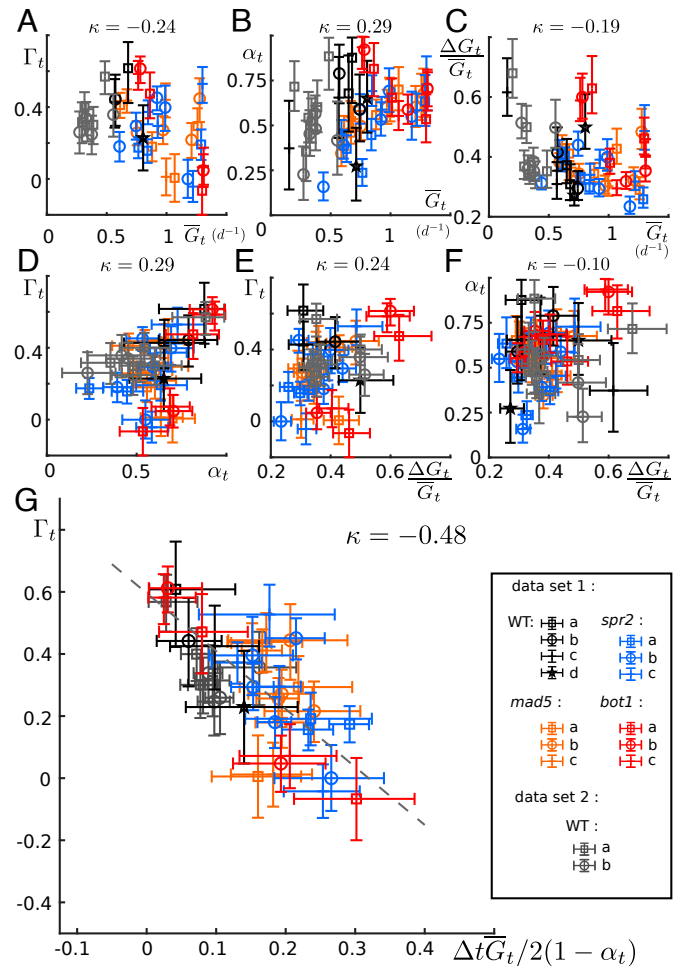


**Fig. 6.** Relations between parameters of growth (fluctuations). (A–F) Pairwise scatter plots of all growth parameters. (A–C) Temporal correlation coefficient  $\Gamma_t$ , exponent of spatial fluctuations  $\alpha_t$ , and dimensionless amplitude of spatial fluctuations,  $\Delta G_t/\bar{G}_t$ , respectively, as function of average growth  $\bar{G}_t$ . (D and E) Temporal correlation coefficient,  $\Gamma_t$ , as function of exponent of spatial fluctuations,  $\alpha_t$ , and dimensionless amplitude of spatial fluctuations,  $\Delta G_t/\bar{G}_t$ , respectively. (F) Exponent of spatial fluctuations,  $\alpha_t$ , as function of their dimensionless amplitude,  $\Delta G_t/\bar{G}_t$ . (G) Test of the coupling between temporal and spatial fluctuations, as resulting from fluctuation stretching. Temporal correlation coefficient  $\Gamma_t$  as a function of the combination  $\Delta t \bar{G}_t (1 - \alpha_t)/2$  where  $\Delta t = 1d$  is the time step of live imaging. The dashed line corresponds to a linear fit,  $\Gamma_t = \beta_0 + \beta_1 \Delta t \bar{G}_t (1 - \alpha_t)/2$ , with fit parameters  $\beta_0 = 0.596 \pm 0.024$  and  $\beta_1 = -1.87 \pm 0.15$ . The analysis of the fit residuals supports a deterministic relation between the two; see *SI Appendix, Supplementary Note*. In all panels, error bars show the 90% CI; black, blue, orange, and red symbols correspond to wild-type, *spr2*, *mad5*, and *bot1* sepals from dataset 1, respectively, while gray symbols correspond to wild-type sepals from dataset 2. Kendall’s correlation coefficient,  $\kappa$ , is shown above each plot.

support the hypothesis of a deterministic relation between  $\Gamma_t$  and  $\Delta t \overline{G}_t(1 - \alpha_t)/2$  and therefore indicate that fluctuation stretching is at play in growing sepals.

## Discussion

Our analysis provides evidence that growth stretches temporally persistent fluctuations: While no clear pairwise relation could be made among the different growth parameters (Fig. 6 A–F), the clear trend of panel G suggests that the persistence time can be deduced from space correlations and tissue growth. This phenomenon explains why higher correlation between cells (higher spatial correlations) may induce more variable organ shape and size (26). Fluctuation stretching gives a prominent role to the persistence time (correlation time) in controlling spatial correlations in the tissue. Any mechanism that would decrease persistence time would reduce spatial correlations and, as a consequence, variability of organ contours. Accordingly, reducing persistence time would yield robust morphogenesis.

Surprisingly, we found that the temporal correlation coefficient,  $\Gamma_t$ , is generally not much smaller than unity, implying that the persistence time,  $\tau_t$ , is not much smaller than the time scale of growth  $1/\overline{G}_t$ . This might be specific to plants. The cell wall sets the local growth rate, and, at the same time, is remodeled at the pace of growth, so that the persistence time of fluctuations of cell wall properties is related to the time scale of growth. It would be worthwhile to extend our study to expanding animal tissues imaged live such as the imaginal disc of the fruit fly (41). In animal tissues that undergo convergent extension, we would expect fluctuation stretching to operate only in the direction of extension, and so spatial correlations to be highly anisotropic.

As a consequence of fluctuation stretching, the level of time persistence, or more rigorously its product with average growth rate  $\tau \overline{G}$ , has a strong impact on variability of organ shape and size variability. Indeed, the shape and size of an organ result from the growth of its cells (or of its subcellular elements) integrated over time. If cell growth has a random component, well-defined shape and size may still be obtained through spatiotemporal averaging (26), the cancelation of random effects over large samples (number of cells or time points)—a local excess of growth may be compensated by lower growth later or elsewhere in the tissue. Higher temporal or spatial correlations reduce spatiotemporal averaging since an excess of growth is less likely to be compensated. Accordingly, higher temporal persistence (scaled with growth rate) reduces the robustness of organ shape and size.

We found a higher spatial extent of correlations (higher  $\alpha_t$ ) in mutant genotypes, suggesting higher  $\tau \overline{G}$ . This means that these mutants potentially have more variable shapes or are less robust to perturbations, consistent with the observation that the width of sepals in *bot1* and *spr2* varies more with trichome number in WT plants (31). We previously predicted that variability of organ contours is minimal for a well-defined level of feedback from mechanical stress to cellulose synthesis (27), leading to the hypothesis that in wild-type sepals the level of mechanical feedback is optimized so as to reduce variability of sepal shape, compared to mutants with lower (*bot1*) or with higher (*spr2*) mechanical feedback. This level of mechanical feedback also corresponds to a minimum of the persistence time of fluctuations (scaled with average growth rate),  $\tau \overline{G}$ , highlighting the importance of this factor in setting the robustness of organ shape and size.

Fluctuation stretching is a kinematic phenomenon: Properties of cells or of regions of cells are carried (advected) by tissue growth and deformation; the persistence time of these properties sets how they are carried to larger or smaller spatial scales, in the case of tissue expansion or tissue shrinkage, respectively. This kinematic phenomenon applies to any type of property or field as long as it is carried by tissue growth and deformation, such as protein concentrations in cells. Although fluctuation stretching not only applies to scalar quantities but also to vector fields (e.g., cell polarity) or tensorial fields (e.g., organization of cytoskeleton), we limited our study to a scalar (areal growth) and did not consider growth anisotropy to avoid the difficulty of taking into account the curved geometry of sepals. Mathematical formalisms such as quasiconformal transforms (42) may nevertheless help to circumvent this difficulty. In the case of complex advective flows, effects associated with corotation may arise for nonscalar fields. Advection also applies to nonrandom properties, in line with theoretical models of polarity fields showing that a combination of morphogens, advection, and time persistence can reproduce the shapes of leaves (43), or with models of leaf vasculature that show that areole (region delimited by veins) shape is advected by leaf growth (44).

Altogether, our work sheds light on the role of persistence time, that is the memory of previous states of a given property, in the robustness of morphogenesis. The investigation of spatiotemporal fluctuations may provide a broad avenue to characterize organ development.

## Datasets and Methods

**Model for Fluctuation Stretching.** We introduced a simple model for the dynamics of a quantity  $\Phi(x, t)$  that varies with position vector,  $x$ , in  $D$ -dimensional Cartesian space and with time,  $t$ . We assumed  $\Phi$  to be advected by tissue growth at rate  $\overline{G}$ , to have a persistence time  $\tau$ , relaxing toward its reference value  $\langle \Phi \rangle$ , and to be driven by a stochastic source  $\xi(x, t)$ , so that

$$\partial_t \Phi(x, t) + \overline{G}/D x \cdot \partial_x \Phi(x, t) = -(\Phi(x, t) - \langle \Phi \rangle)/\tau + \xi(x, t). \quad [4]$$

This equation can be solved as shown in *SI Appendix, Supplementary Note*.

**Experimental Datasets.** In order to reliably analyze fluctuations of growth rate, we chose datasets of sepals imaged with the highest spatial resolution possible among those published. We used live imaging sequences from ref. 32 (dataset 1) and from ref. 31 (dataset 2). Voxel size was  $0.12 \times 0.12 \times 0.50 \mu\text{m}^3$ . All plant lines in these sequences were crosses between *Ws-4* and *Col-0* ecotypes, harboring respectively the microtubule reporter *p35S::GFP-MBD* and the membrane reporter *pUQ10::Lti6b-2xmCherry* (32). The two datasets had slightly different culture conditions (type of lighting). Dataset 1 contained wild-type plants, the *spr2-2* allele of *SPIRAL2* that was originally obtained in a *Col-0* background, the *bot1-7* allele of *Katanin* that was originally obtained in a *Ws-4* background, and the *mad5* allele of *Katanin* that was originally obtained in a *Col-0* background. For *mad5*, addition sequences were obtained in parallel to those already published in ref. 32. All data can be found here: <https://doi.org/10.5281/zenodo.11105905>.

**Segmentation.** For sepals not already processed in refs. 31 and 32, cells of the abaxial epidermis were segmented and tracked in time using MorphoGraphX (45). A triangular mesh was obtained for the outer organ surface in which cells were identified and well-delimited.

**Computation of Growth Rates.** We aimed at analyzing fluctuations of cell relative areal growth rates tangentially to the sepal and therefore to get rid of the curvature of the outer surface of cells. To do so, we redefined the surface of cells from the linear interpolation of their contours by a flat surface. Areal growth rate was computed from the cell surface area at successive time steps.

At time  $t$ , each cell is labeled by an index  $i$  and has surface area  $S_{i,t}$ . Cell  $i$  may divide between  $t$  and  $t + 1$ ; the set  $J_{i,t}$  contains the labels of all daughters of cell  $i$  at time  $t + 1$  ( $J_{i,t}$  is reduced to a single label if cell  $i$  has not divided). We only consider cells which or whose daughters remain in the segmented region from  $t$  to  $t + 1$ . The areal growth rate of the cell  $i$  at a time  $t$  is then defined as

$$G_{i,t} = \left( \sum_{j \in J_{i,t}} S_{j,t+1} \right) / S_{i,t} - 1. \quad [5]$$

Average (tissular) growth is in turn defined as  $\bar{G}_t = (\sum_i \sum_{j \in J_{i,t}} S_{j,t+1}) / (\sum_i S_{i,t}) - 1$ .

**CFTs.** The Fourier harmonics are built from a coarse and discrete version of the Laplace operator. To compute this operator we triangularized cell surfaces using the "MESH2D" matlab algorithm (46, 47). More details can be found in [SI Appendix, Supplementary Note](#). The CFT  $\hat{G}_{k,t}$  of cell relative areal growth gives the weights by which growth is decomposed over the harmonics  $e_k$  of the CFT. In this paper, the definition of the CFT differs from the one in ref. 38 by a prefactor  $1/\sqrt{S_t}$  where  $S_t$  is the total surface area. This change simplifies the interpretation of Fourier spectra: The coefficients have the same physical dimension as the original signal and the first coefficient is the average of the signal.

**Scaling Exponent and Amplitude of Fluctuations.** We quantified spatial correlations in the tissue by fitting the spectral density with a power law. To do so, we assumed a Gaussian distribution for the CFT, centered around 0 with a SD verifying,

$$\sigma_{k,t} = \Delta G_t q_k^{-\alpha_t} / \sqrt{\sum_l q_l^{-2\alpha_t}}, \quad [6]$$

where  $\Delta G_t$  and the scaling exponent  $\alpha_t$  are the fit parameters characterizing respectively the amplitude and the extent of spatial correlation of growth fluctuations. For the fit, we used statistical inference as detailed in [SI Appendix, Supplementary Note](#). Doing so, we estimated a probability for the parameters  $\Delta G_t$  and  $\alpha_t$ , their expected value, their SE, and median values. We also estimated the 90% CI, from the fifth to the ninety-fifth percentiles.

**Temporal Correlations.** We estimated temporal correlations of relative areal growth in considering cell growth  $G_{i,t}$  from  $t$  to  $t + 1$  and cell growth  $G_{J_{i,t},t+1}$  from  $t + 1$  to  $t + 2$ .  $G_{J_{i,t},t+1}$  is simply the areal growth rate from  $t$  to  $t + 1$  of the descendants of the cell  $i$  in the segmentation at  $t$ :

$$G_{J_{i,t},t+1} = \frac{\sum_{j \in J_{i,t}} \sum_{l \in J_{j,t+1}} S_{l,t+2}}{\sum_{j \in J_{i,t}} S_{j,t+1}} - 1. \quad [7]$$

To avoid any bias due to systematic variation of growth at organ scale (32), we used the detrended cell growth  $\delta G_{i,t}$ , which can be defined by subtracting average growth in a local neighborhood from cell growth; see [SI Appendix, Supplementary Note](#). Temporal correlations were computed as Kendall's correlation coefficient  $\Gamma_t$  of  $\delta G_{i,t}$  and  $\delta G_{J_{i,t},t+1}$ . Kendall's correlation coefficient is rank-based and so is less sensitive to outliers (39). We used bootstrapping to obtain CI and uncertainties.

We note that  $\Gamma_t$  tends to be underestimated: A positive error on  $S_{J_{i,t},t+1}$  leads to an overestimation of  $\delta G_{i,t}$  and an underestimation of  $\delta G_{J_{i,t},t+1}$ , inducing a negative correlation between  $\delta G_{i,t}$  and  $\delta G_{J_{i,t},t+1}$ . This may explain the few negative values of  $\Gamma_t$ . We found this negative bias to be stronger when we defined growth from the cell's outer surface area, leading us to use the interpolation of cell contours instead (see above).

**Comparing Genotypes.** To describe the impact of mutations or culture conditions on growth parameters, we compared tissues at equivalent developmental stages. We first synchronized all the live imaging sequences from a dataset by building upon the approach developed in ref. 40. We considered the curves representing organ width vs. time for every sepal and determined the time delays ensuring the best superposition between width vs. time curves, leading to a corrected time  $\bar{T}_t$ . We checked that this temporal alignment was consistent with stages of guard cell differentiation, indicating that sepal width is a good proxy of developmental stage in the genotypes/conditions that we studied. We defined the mean shift of a quantity  $\Phi_t$  as

$$\mathcal{D}_\Phi = \frac{\sum_{n',t'} \sum_{n,t} W_{t',t}^{(n',n)} (\Phi_{t'}^{(n')} - \Phi_t^{(n)})}{\sum_{n',t'} \sum_{n,t} W_{t',t}^{(n',n)}}, \quad [8]$$

where  $n'$  and  $n$  label the pair of sepals compared (e.g., one mutant and the reference wild-type) and  $t'$  and  $t$  correspond to the time in the sequence of live-imaging of those two sepals. The sums  $\sum_{n',t'}$  and  $\sum_{n,t}$  are over all sequences of the mutant and the WT, respectively.  $W_{t',t}^{(n',n)}$  gives the weights at which each pair is considered. A weight differs from 0 only if the values of synchronized times  $\bar{T}_t$  of the pair are close; see [SI Appendix, Supplementary Note](#) for details.  $\mathcal{D}_\Phi$  quantifies how much, in average, the quantities  $\Phi_t$  for the mutants (or for WT in dataset 2) are shifted from the reference WT.

**Data, Materials, and Software Availability.** Matlab code and segmented live imaging data and results have been deposited in Zenodo (48). Previously published data were used for this work (31, 32).

**ACKNOWLEDGMENTS.** This work has been supported by the AgreeSkills+ fellowship programme, which has received funding from the European Union's Seventh Framework Programme under grant agreement number FP7-609398 (AgreeSkills+ contract, to A.F.), by the Department of Plant Biology and Breeding at Institut national de recherche pour l'agriculture, l'alimentation et l'environnement, and by Institut Universitaire de France (to A.B.).

Author affiliations: <sup>a</sup>Reproduction et Développement des Plantes, Université de Lyon, Ecole normale supérieure de Lyon, Université Claude Bernard Lyon 1, Institut national de recherche pour l'agriculture, l'alimentation et l'environnement, CNRS, 69364 Lyon Cedex 07, France; <sup>b</sup>Laboratoire d'Hydrodynamique, CNRS, Ecole polytechnique, Institut Polytechnique de Paris, 91128 Palaiseau Cedex, France; <sup>c</sup>Laboratoire de Physique Théorique et Modèles Statistiques, CNRS, Université Paris-Saclay, 91405 Orsay, France; <sup>d</sup>Institute of Nuclear Agricultural Sciences, Key Laboratory of Nuclear Agricultural Sciences of Ministry of Agriculture and Zhejiang Province, College of Agriculture and Biotechnology, Zhejiang University, Hangzhou 310058, Zhejiang, China; <sup>e</sup>Weill Institute for Cell and Molecular Biology and Section of Plant Biology, School of Integrative Plant Science, Cornell University, Ithaca, NY 14853; and <sup>f</sup>Department of Mathematics, Stockholm University, 106 91 Stockholm, Sweden

1. L. Hong *et al.*, Heterogeneity and robustness in plant morphogenesis: From cells to organs. *Annu. Rev. Plant Biol.* **69**, 469–495 (2018).
2. D. S. Banerjee, A. Munjal, T. Lecuit, M. Rao, Actomyosin pulsation and flows in an active elastomer with turnover and network remodeling. *Nat. Commun.* **8**, 1121 (2017).
3. Y. Long *et al.*, Cellular heterogeneity in pressure and growth emerges from tissue topology and geometry. *Curr. Biol.* **30**, 1504–1516 (2020).
4. S. Armon, M. Moshe, E. Sharon, The multiscale nature of leaf growth fields. *Commun. Phys.* **4**, 1–7 (2021).
5. N. Gorfinkiel, S. Schamberg, G. B. Blanchard, Integrative approaches to morphogenesis: Lessons from dorsal closure. *Genesis* **49**, 522–533 (2011).
6. N. Gorfinkiel, G. B. Blanchard, Dynamics of actomyosin contractile activity during epithelial morphogenesis. *Curr. Opin. Cell Biol.* **23**, 531–539 (2011).
7. R. Levayer, T. Lecuit, Oscillation and polarity of E-cadherin asymmetries control actomyosin flow patterns during morphogenesis. *Dev. Cell* **26**, 162–175 (2013).
8. M. Rauzi, P. Verant, T. Lecuit, P.-F. Lenne, Nature and anisotropy of cortical forces orienting drosophila tissue morphogenesis. *Nat. Cell Biol.* **10**, 1401–1410 (2008).
9. R. M. Herrera-Perez, C. Cupo, C. Allan, A. B. Dagle, K. E. Kasza, Tissue flows are tuned by actomyosin-dependent mechanics in developing embryos. *PRX Life* **1**, 013004 (2023).
10. J. R. Chubb, Symmetry breaking in development and stochastic gene expression. *Wiley Interdiscip. Rev. Dev. Biol.* **6**, e284 (2017).
11. F. Corson, L. Couturier, H. Rouault, K. Mazouni, F. Schweisguth, Self-organized notch dynamics generate stereotyped sensory organ patterns in *Drosophila*. *Science* **356**, eaai7407 (2017).
12. B. Moulia, S. Douady, O. Hamant, Fluctuations shape plants through proprioception. *Science* **372**, ea6c868 (2021).
13. T. Kalmar *et al.*, Regulated fluctuations in nanog expression mediate cell fate decisions in embryonic stem cells. *PLoS Biol.* **7**, e1000149 (2009).
14. D. Streibinger *et al.*, Endogenous fluctuations of OCT4 and SOX2 bias pluripotent cell fate decisions. *Mol. Syst. Biol.* **15**, e9002 (2019).

15. S. Pouteau, C. Albertini, An assessment of morphogenetic fluctuation during reproductive phase change in *Arabidopsis*. *Ann. Bot.* **107**, 1017–1027 (2011).
16. L. Corrales-Guerrero *et al.*, Spatial fluctuations in expression of the heterocyst differentiation regulatory gene *hetR* in *Anabaena* filaments. *PLoS Genet.* **11**, e1005031 (2015).
17. O. Agam, E. Braun, Universal calcium fluctuations in hydra morphogenesis. *Phys. Biol.* **20**, 066002 (2023).
18. D. Krotov, J. O. Dubuis, T. Gregor, W. Bialek, Morphogenesis at criticality. *Proc. Natl. Acad. Sci. U.S.A.* **111**, 3683–3688 (2014).
19. R. Belousov, A. Jacobo, A. J. Hudspeth, Fluctuation theory in space and time: White noise in reaction-diffusion models of morphogenesis. *Phys. Rev. E* **98**, 052125 (2018).
20. V. Kasatkin, A. Prochiantz, D. Holcman, Morphogenetic gradients and the stability of boundaries between neighboring morphogenetic regions. *Bull. Math. Biol.* **70**, 156–178 (2008).
21. K. D. Irvine, B. I. Shraiman, Mechanical control of growth: Ideas, facts and challenges. *Development* **144**, 4238–4248 (2017).
22. V. Mirabet, P. Das, A. Boudaoud, O. Hamant, The role of mechanical forces in plant morphogenesis. *Annu. Rev. Plant Biol.* **62**, 365–385 (2011).
23. G.-J. Jason Gao, M. C. Holcomb, J. H. Thomas, J. Blawdziewicz, Embryo as an active granular fluid: Stress-coordinated cellular constriction chains. *J. Phys. Condens. Matter* **28**, 414021 (2016).
24. D. R. Hipfner, S. M. Cohen, Connecting proliferation and apoptosis in development and disease. *Nat. Rev. Mol. Cell Biol.* **5**, 805 (2004).
25. M. Milán, S. Campuzano, A. García-Bellido, Cell cycling and patterned cell proliferation in the wing primordium of *Drosophila*. *Proc. Natl. Acad. Sci. U.S.A.* **93**, 640–645 (1996).
26. L. Hong *et al.*, Variable cell growth yields reproducible organ development through spatiotemporal averaging. *Dev. Cell* **38**, 15–32 (2016).
27. A. Fruleux, A. Boudaoud, Modulation of tissue growth heterogeneity by responses to mechanical stress. *Proc. Natl. Acad. Sci. U.S.A.* **116**, 1940–1945 (2019).
28. O. K. Damavandi, D. K. Lubensky, Statistics of noisy growth with mechanical feedback in elastic tissues. *Proc. Natl. Acad. Sci. U.S.A.* **116**, 5350–5355 (2019).
29. W. Li, Expansion-modification systems: A model for spatial  $1/f$  spectra. *Phys. Rev. A* **43**, 5240–5260 (1991).
30. A. R. Liddle, D. H. Lyth, *Cosmological Inflation and Large-Scale Structure* (Cambridge University Press, 2000).
31. N. Hervieux *et al.*, Mechanical shielding of rapidly growing cells buffers growth heterogeneity and contributes to organ shape reproducibility. *Curr. Biol.* **27**, 3468–3479 (2017).
32. N. Hervieux *et al.*, A mechanical feedback restricts sepal growth and shape in *Arabidopsis*. *Curr. Biol.* **26**, 1019–1028 (2016).
33. M. Nakamura, J. J. Lindeboom, M. Saltini, B. M. Mulder, D. W. Ehrhardt, SPR2 protects minus ends to promote severing and reorientation of plant cortical microtubule arrays. *J. Cell Biol.* **217**, 915–927 (2018).
34. M. Uyttewaal *et al.*, Mechanical stress acts via katanin to amplify differences in growth rate between adjacent cells in *Arabidopsis*. *Cell* **149**, 439–451 (2012).
35. O. Hamant *et al.*, Developmental patterning by mechanical signals in *Arabidopsis*. *Science* **322**, 1650–1655 (2008).
36. A. Sampathkumar *et al.*, Subcellular and supracellular mechanical stress prescribes cytoskeleton behavior in *Arabidopsis* cotyledon pavement cells. *eLife* **3**, e01967 (2014).
37. A. R. Paredez, C. R. Somerville, D. W. Ehrhardt, Visualization of cellulose synthase demonstrates functional association with microtubules. *Science* **312**, 1491–1495 (2006).
38. A. Fruleux, A. Boudaoud, Cellular Fourier analysis for geometrically disordered materials. *Phys. Rev. Res.* **3**, 023036 (2021).
39. C. Croux, C. Dehon, Influence functions of the Spearman and Kendall correlation measures. *Stat. Methods Appl.* **19**, 497–515 (2010).
40. C. Mollier *et al.*, Spatial consistency of cell growth direction during organ morphogenesis requires CELLULOSE SYNTHASE INTERACTIVE<sub>1</sub>. *Cell Rep.* **42**, 112689 (2023).
41. S. Aldaz, L. M. Escudero, M. Freeman, Live imaging of *Drosophila* imaginal disc development. *Proc. Natl. Acad. Sci. U.S.A.* **107**, 14217–14222 (2010).
42. D. J. Cislo, A. Pavlopoulos, B. I. Shraiman, A “morphogenetic action” principle for 3D shape formation by the growth of thin sheets. *arXiv [Preprint]* (2023). <https://arxiv.org/abs/2302.07839> (Accessed 13 May 2024).
43. E. E. Kuchen *et al.*, Generation of leaf shape through early patterns of growth and tissue polarity. *Science* **335**, 1092–1096 (2012).
44. Y. Bar-Sinai *et al.*, Mechanical stress induces remodeling of vascular networks in growing leaves. *PLoS Comput. Biol.* **12**, e1004819 (2016).
45. P. B. de Reuille *et al.*, MorphoGraphX: A platform for quantifying morphogenesis in 4D. *eLife* **4**, e05864 (2015).
46. D. Engwirda, “Unstructured mesh methods for the navier-stokes equations,” Undergraduate Thesis, School of Engineering, University of Sydney, 2005.
47. D. Engwirda, “Locally optimal Delaunay-refinement and optimisation-based mesh generation” PhD Thesis, School of Mathematics and Statistics, University of Sydney, 2014.
48. A. Fruleux, Growth couples temporal and spatial fluctuations of tissue properties during morphogenesis. Zenodo. <https://doi.org/10.5281/zenodo.11105905>. Deposited 13 May 2024.